

This is the accepted manuscript made available via CHORUS. The article has been published as:

Spin waves above and below the Verwey transition in $\text{TbBaFe}_{2}\text{O}_{5}$

Daniel M. Pajerowski, Daniel K. Pratt, Steven E. Hahn, Wei Tian, Garrett E. Granroth,
Alexander I. Kolesnikov, Alexey A. Taskin, Yoichi Ando, and Robert J. McQueeney

Phys. Rev. B **101**, 064418 — Published 18 February 2020

DOI: [10.1103/PhysRevB.101.064418](https://doi.org/10.1103/PhysRevB.101.064418)

Disclaimer: This manuscript has been authored by UT-Battelle, LLC under Contract No. DE-AC05-00OR22725 with the U.S. Department of Energy. The United States Government retains and the publisher, by accepting the article for publication, acknowledges that the United States Government retains a non-exclusive, paid-up, irrevocable, world-wide license to publish or reproduce the published form of this manuscript, or allow others to do so, for United States Government purposes. The Department of Energy will provide public access to these results of federally sponsored research in accordance with the DOE Public Access Plan (<http://energy.gov/downloads/doe-public-access-plan>).

Spin waves above and below the Verwey transition in TbBaFe₂O₅

Daniel M. Pajerowski,^{1,*} Daniel K. Pratt,² Steven E. Hahn,¹ Wei Tian,¹ Garrett E. Granroth,¹

Alexander I. Kolesnikov,¹ Alexey A. Taskin,³ Yoichi Ando,³ and Robert J. McQueeney⁴

¹*Neutron Scattering Division, Oak Ridge National Laboratory, Oak Ridge, TN 37831, USA*

²*NIST Center for Neutron Research, National Institute of Standards and Technology, Gaithersburg, Maryland 20899, USA*

³*Physics Institute II, University of Cologne, 50937 Koeln, Germany*

⁴*Ames Laboratory, US DOE, Iowa State University, Ames, Iowa 50011, USA*

(Dated: January 31, 2020)

TbBaFe₂O_{5+ δ} (TBFO) is a mixed valence compound with an antiferromagnetic order ($T_N = 450$ K) that changes along with the crystal structure and conductivity upon cooling below a Verwey-like transition ($T_V = 280$ K). This type of double-cell-layered-perovskite is useful to study putative charge ordering in fractional valence systems because the crystal structure develops unique sites for the different valence states. While the evolution of the static magnetic structure in the different charge ordered states of TBFO is known, in this study we investigate the effect of charge ordering on the magnetic interactions. Dispersive magnetic excitations measured using single crystal inelastic neutron scattering experiments at $T = 4$ K $< T_V$ and $T = 320$ K $> T_V$ are modeled with linear-spin-wave-theory to extract anisotropy and superexchange parameters. Below T_V , we observe a sizable magnon gap due to an easy-axis magnetic anisotropy that closes above T_V due to the evolution of easy-plane anisotropy. The magnetic interactions are found to be highly three-dimensional and change across T_V . Above T_V , where the conductivity is greater, a damping term is required to model the spin waves that suggests a coupling to valence fluctuations.

I. INTRODUCTION

Magnetic transition metal oxides (TMOs) are a key-stone of solid-state physics, and they host a varied array of fundamental and technological properties [1]. As lodestones, the ferritic TMO magnetite having chemical formula Fe₃O₄ introduced humanity to magnetism, then to ferrimagnetism, Mott insulators, and more and has proven a model material challenging our understanding even to the modern age [2, 3]. Below the magnetic ordering transition of magnetite ($T_C = 850$ K), [4] there is the Verwey transition ($T_V = 125$ K) that is characterized by a change in the material properties including the resistivity, crystal structure, and magnetism [2]. This Verwey transition has been the subject of intense scrutiny, and an evolving understanding over the years. While some aspects of Verwey's original model of charge ordering driving the different response above and below T_V are generally accepted, the degree of electron transfer and underlying mechanisms continue to be the subject of debate [3]. Even the simple chemical formula of Fe₃O₄ for magnetite that is more accurately written as FeFe₂O₄ to show the crystallographically distinct Fe sites in the cubic inverse spinel structure illustrates the hidden subtleties. Among the experimental difficulties for magnetite are that crystallographic determination of site-specific parameters is not possible, as the valence mixing takes places between iron ions on the B-site. This and other difficulties motivate the search for compounds showing similar Verwey behavior that may support simpler models.

Other materials have analogous Verwey(-like) phase transitions, of which one class is the double-cell, layered

perovskites (DCLPs) $R^{3+}\text{Ba}^{2+}M_2^{2.5+}\text{O}_5^{2-}$ (R = rare-earth metal, M = transition metal) [5]. These DCLPs are attractive as a model system to investigate because their crystal structure develops two unique transition metal sites in the low-temperature state, which helps remove ambiguity regarding potential charge disproportionation. Of these DCLPs, the TbBaFe₂O_{5+ w} (TBFO) compound may be fabricated with controllable stoichiometry and was therefore subsequently studied with an array of experiments to generate a detailed description of the electronic and magnetic properties [6]. Upon cooling, phase transitions are observed in TBFO at the Nel temperature of $T_N = 450$ K where a magnetostrictive distortion in the crystal structure is detected, and at the Verwey temperature of $T_V = 280$ K where an additional hysteretic crystal structure distortion concomitant with changes in the direction and magnitude of the magnetic moments, iron oxidation states (charge disproportionation), and conductivity are seen. Of the bulk properties, the most striking change is the precipitous drop in the conductivity below T_V [6].

These changes in the crystal and magnetic structures in TBFO have been studied in detail [6]. Above T_V in the fractional valence (FV) state, the TBFO has a formal valence of Fe^{2.5+}. Between T_V and T_N at 420 K the crystal structure is orthorhombic $Pmmm$ with one unique crystallographic iron site and a magnetic moment of $\mu_{Fe} = [0, 1.38 \mu_B, 0.40 \mu_B]$ refined from neutron diffraction. The magnetic structure is antiferromagnetic for the b-axis components and doubles the nuclear crystallographic cell along all three directions, while the c-axis component was refined as ferromagnetic; in the a-b plane the nearest neighbors are antiferromagnetically oriented, while along the c-axis the intra-layer moments are antiferromagnetic and the inter-layer moments are ferromagnetically ori-

* pajerowskidm@ornl.gov

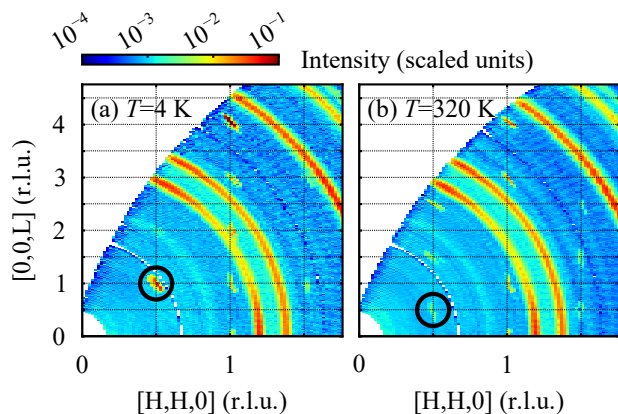


FIG. 1. Magnetic neutron diffraction of TBFO. Elastic scattering reciprocal space map with the INS unit cell using $E_i = 120$ meV and integrating $dE = [-5 \text{ meV}, 5 \text{ meV}]$ for (a) $T = 4$ K charge ordered (CO) phase with $(\frac{1}{2}, \frac{1}{2}, 1)$ magnetic Bragg peak circled and (b) $T = 320$ K fractional valence (FV) phase with $(\frac{1}{2}, \frac{1}{2}, \frac{1}{2})$ magnetic Bragg peak circled.

ented, Figure 2 (c). Below T_V in the charge ordered (CO) state there is a descent in symmetry to orthorhombic $Pmna$ and two unique crystallographic iron sites with striped charge ordering develop having $\text{Fe}^{(2.5+)+\epsilon}$ and $\text{Fe}^{(2.5+)-\epsilon}$ with neutron diffraction refined magnetic moments of $\mu_{Fe} = [0, 4.15 \mu_B, 0]$ and $\mu_{Fe} = [0, 3.65 \mu_B, 0]$, respectively. Aside from the magnetic moment disproportionation, there is an additional change from the high-temperature magnetic structure whereby the inter-layer moments become antiferromagnetically aligned, Fig. 2 (d). Furthermore, for highly stoichiometric TBFO with oxygen excess $w < 0.002$, an additional phase transition at $T^* = 310$ K precedes the stripe charge ordering transition at T_V and is associated with a checkerboard charge ordering [7].

While neutron diffraction can give the static magnetic structure, inelastic neutron scattering (INS) is sensitive to the interactions between magnetic ions. Given the orbitally selective nature of charge disproportionation, it is expected that the magnetic interactions are sensitive to charge ordering. Thus, the magnetic interactions and how they change in different charge ordered and charge melted phases may be used to check models of the electronic structure. To this end, a polycrystalline sample of the DCLP compound $\text{YBaFe}_2\text{O}_{5+w}$ (YBFO) was studied with INS to investigate the spin waves and extract the spin Hamiltonian [8]. That YBFO analysis was able to extract Heisenberg superexchange parameters for the low-temperature CO state, and an average exchange energy of the high-temperature FV state (therein referred to as valence mixed) where significant damping of the spin waves was reported.

In the following section, we use INS from single crystals to quantify the spin wave excitations of TBFO in the charge-melted antiferromagnetic FV phase between T^* and T_N ($T = 320$ K) and in the stripe-charge or-

TABLE I. Crystallographic unit cells and magnetic ordering wave-vectors for TBFO use for INS compared to the formal cells.

	INS CO	INS FV	CO [6]	FV [6]
a (Å)	3.94	3.94	8.085	3.945
b (Å)	3.94	3.94	3.850	3.933
c (Å)	7.6	7.6	7.553	7.587
k (r. l. u.)	$(\frac{1}{2}, \frac{1}{2}, 0)$	$(\frac{1}{2}, \frac{1}{2}, \frac{1}{2})$	$(0, \frac{1}{2}, 0)$	$(\frac{1}{2}, \frac{1}{2}, \frac{1}{2})$
T (K)	4	320	70	350

dered Verwey CO phase below T_V ($T = 4$ K). First, the elastic scattering is confirmed to be consistent with the reported structures, aside from one small modification, and the parameter set is defined. Then, models of the magnetic interactions for the CO and FV phases are obtained by fitting to the measured neutron spectra using linear-spin-wave-theory (LSWT) to extract nearest-neighbor superexchange parameters and magnetocrystalline anisotropy. In addition to changes in the LSWT parameters across T_V , the FV phase shows spin wave damping. To conclude, the results are summarized in the context of the existing literature and future directions to build on these results. Technical details are reported in Appendix A.

II. RESULTS AND DISCUSSION

A. Magnetic structure, unit cells, and model interactions

As described in the introduction, TBFO has two distinct magnetic structures. While the INS samples are single crystals, a twinning of orthorhombic domains in the a-b plane is present at 420 K as the lattice parameters in the basal plane are within 0.15% from $a = 3.94596(7)$ and $b = 3.93986(7)$. Therefore, INS data are indexed using a pseudo-tetragonal cell. The relationship between the formal structures and the INS cell is summarized in Table I. At $T = 4$ K in the CO phase, the $\mathbf{Q} = (\frac{1}{2}, \frac{1}{2}, 0)$ family of reflections indexed in the INS cell is observed with the neutron spectrometer, Fig. 1 (a). At $T = 320$ K in the FV phase, the $\mathbf{Q} = (\frac{1}{2}, \frac{1}{2}, \frac{1}{2})$ family of reflections indexed in the INS cell is observed with the neutron spectrometer, Fig. 1 (b).

The magnetic structure for the CO phase at $T = 4$ K is shown in Fig. 2 (a) along with the model superexchange interactions J_a coupling spins along the a-axis, J_b coupling spins along the b-axis, J_{cS} coupling spins across the shorter inter-layer c-axis spin spacing that spans the oxygen linked iron layers, and J_{cL} coupling spins across the longer intra-layer c-axis spin spacing that spans the oxygen vacancies between iron layers. For the FV state at $T = 320$ K, Fig. 2 (b), the magnetic structure used here for the spin dynamics does not include the ferromagnetic c-axis magnetic moment that was obtained from FV

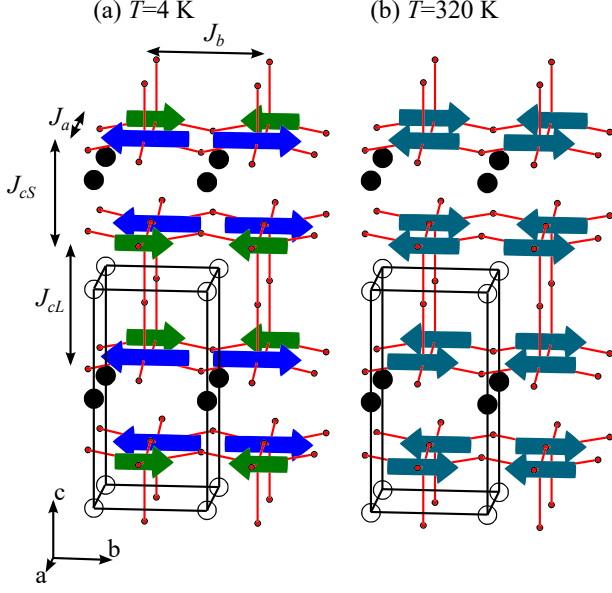


FIG. 2. Magnetic structure, and model interactions of TBFO. Magnetic structures are shown for the (a) CO phase where shorter green arrows denote $\text{Fe}^{(2.5+)+\epsilon}$ and longer blue arrows denote $\text{Fe}^{(2.5+)-\epsilon}$ magnetic moments, and the (b) FV $\text{Fe}^{2.5+}$ phase. Red lines illustrate iron to oxygen bonds, with O^{2-} ions shown as small red circles. Black circles denote Tb^{3+} and white circles denote Ba^{2+} . Unit cells used for analysis and discussion of the INS data are shown as black boxes. Model exchange interactions are illustrated with double-ended arrows. Illustrations in (a) and (b) are based upon VESTA [9] outputs.

neutron diffraction data [6]. The motivation for this difference is that the c-axis magnetization does not have any such increase when warming across TV [7] and moreover the introduction of a c-axis magnetic moment would require an additional irreducible representation to the magnetic structure. The same parameterization of the spin Hamiltonian is used for the FV state as in the CO state.

The LSWT dynamics are based upon a Heisenberg Hamiltonian with single-ion anisotropy

$$H = -\frac{1}{2} \sum_{\langle i,j \rangle} J_{ij} \mathbf{S}_i \cdot \mathbf{S}_j + D_\alpha \sum_i (S_i^\alpha)^2, \quad (1)$$

where J_{ij} is the superexchange energy between spins \mathbf{S}_i and \mathbf{S}_j , $\langle i, j \rangle$ indicates that the sum is only over nearest neighbors, and D_α is the single-ion anisotropy energy for which α may be along the a-, b-, or c-axis. From the refined magnetic structures, the anisotropy quantization defining the easy-axis is along the crystallographic b-axis. For the fractional valence state, $S = 2.25$ is used. For the charge ordered state, $S = 2$ and $S = 2.5$ are used for the $\text{Fe}^{(2.5+)+\epsilon}$ and $\text{Fe}^{(2.5+)-\epsilon}$ ions, respectively. While the degree of charge ordering in TBFO is an open question, the spin values for Fe^{3+} and Fe^{2+} are used to avoid additional confusion and resulting numerical values for the magnetic interactions may be re-scaled with

simple multiplication. We use results from density functional theory (DFT) calculations on the charge ordered phase of YBFO [10] to limit the parameter set used to fit the INS data. The DFT calculations show a dominant nearest neighbor interaction as parameterized here, although we exclude additional longer-range interactions that are present in the YBFO calculations. Those same DFT based YBFO calculations also support the usage of one superexchange energy for Fe^{3+} to Fe^{3+} and Fe^{2+} to Fe^{2+} along the b-axis via the parameter J_b , which reduces the parameter space of the model compared to having unique J_b parameters for both ions. The YBFO DFT superexchange energies of the low-temperature CO ground-state map to the superexchange energies used here as $J_1 = \frac{1}{2} J_{cL} = -12.1$ meV, $J_2 = \frac{1}{2} J_{cS} = -7.4$ meV, $J_4 = \frac{1}{2} J_b = -8.8$ meV, $J_5 = \frac{1}{2} J_b = -8.7$ meV, and $J_6 = \frac{1}{2} J_a = -4.2$ meV, where the factors of 2 are from different definitions of the superexchange Hamiltonian. A total of 12 superexchange energies were considered in the YBFO DFT calculation report, which is an intractable number for spin wave spectra refinement, and the remaining parameters vary between 1.9 meV to -2.5 meV. Although there is one superexchange energy J_b for divalent and trivalent species, the energy of the interactions is modulated by the spin of the species involved.

B. Spin waves at $T = 4$ K, below the Verwey transition

Inelastic neutron scattering of a co-aligned TBFO sample in the HHL scattering plane were performed at $T = 4$ K, below the Verwey transition in the CO phase. Initial investigatory scans were performed with an $E_i = 240$ meV in order to ascertain the energy range of the spin waves. Subsequently, a series of single-crystal rotations with $E_i = 120$ meV were performed to extract intensities proportional to the scattering function $S(\mathbf{Q}, \hbar\omega)$. Data were folded over twin directions and across all zero-momentum planes using the pseudo-tetragonal symmetry of the INS cell. Dispersive excitations were observed to originate at a finite energy offset above the CO antiferromagnetic ordering wave-vector, Fig. 3 (a-c). These data compare well to a LSWT model that is plotted for a visual comparison without any instrumental momentum resolution applied, Fig. 3 (d-f).

In order to model the measured spin waves, these four-dimensional data were integrated over momentum ranges larger than the experimental resolution to extract intensity versus energy. The calculated spin wave spectra were convolved with the instrumental energy resolution for comparison with the experimental data. Eight regions (i to viii) were chosen in order to refine the model Hamiltonian. The extrinsic model parameters include an overall shared scale-factor globally varied across the optimization regions and an independent constant plus linear in energy background term separately varied for each optimization region. Data cuts below 45 meV were

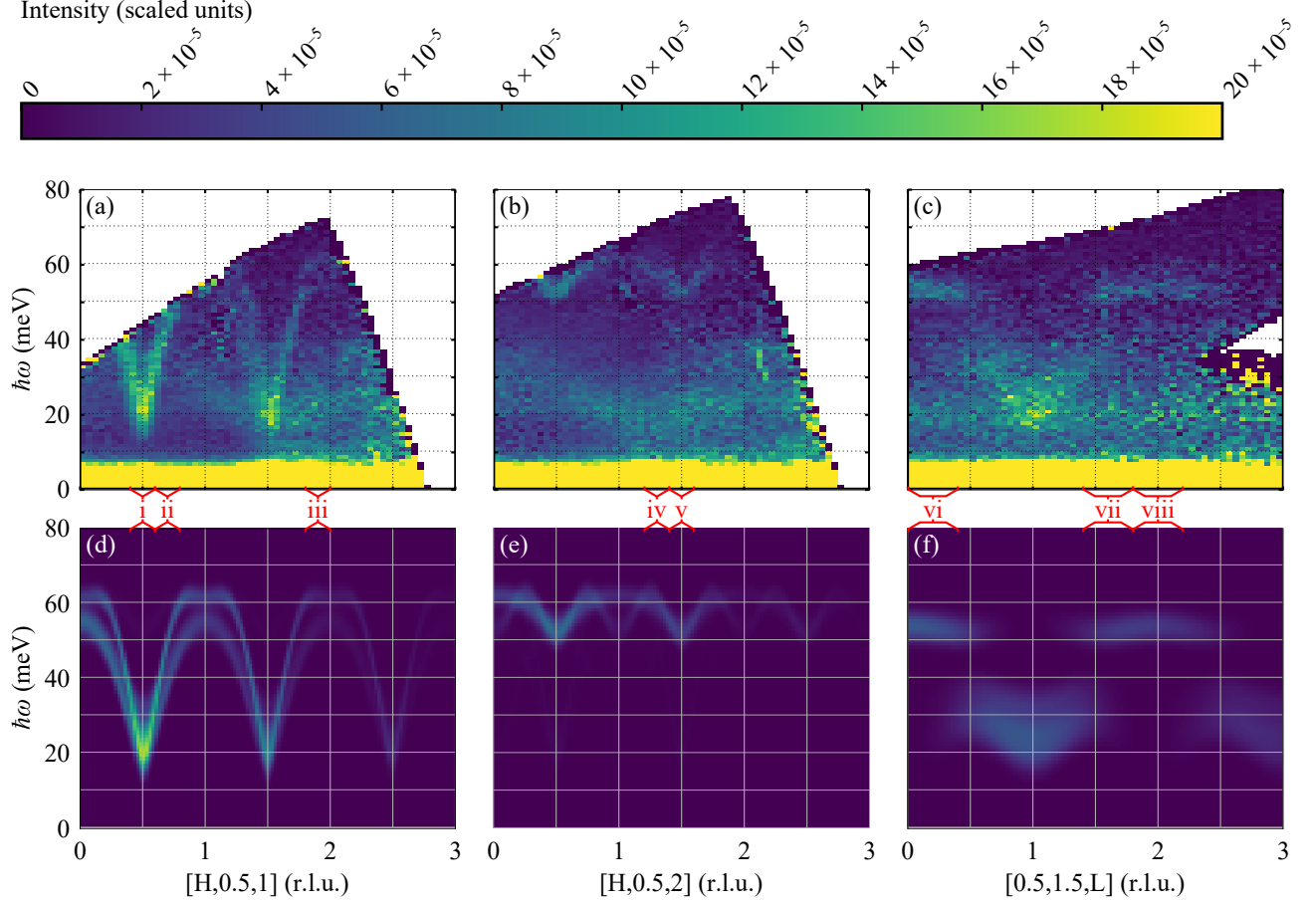


FIG. 3. Neutron scattering function intensity maps of momentum in reciprocal lattice units versus energy transfer at $T = 4$ K for TBFO in the CO phase. Experimental data collected on the SEQUOIA with $E_i = 120$ meV are shown for (a) $L = \text{odd}$ along H such that the interval ranges are $K = [0.4, 0.6]$ r.l.u. and $L = [0.8, 1.2]$ r.l.u., (b) $L = \text{even}$ along H such that $K = [0.4, 0.6]$ r.l.u. and $L = [1.8, 2.2]$ r.l.u., and (c) at the ordering magnetic wave-vector along L such that $H = [0.4, 0.6]$ r.l.u. and $K = [1.4, 1.6]$ r.l.u.. The momenta in the horizontal axis titles are the bin centers for the not-shown directions that reduce the four-dimensional $S(\mathbf{Q}, \hbar\omega)$ to the two-dimensional $S(Q, \hbar\omega)$ shown here. The same regions are shown in panels (d-f) for calculations using the **CO-best-fit** parameters. The sample is twinned in the a-b plane and this twinning is included in the calculated data. The red Roman numerals delineate the regions used for model optimization also shown in Fig. 4.

TABLE II. Linear-spin-wave-theory parameters for TBFO, $T = 4$ K data in the CO phase. The uncertainties are one standard deviation confidence intervals derived from the least-squares model. The χ_r^2 is the reduced chi squared.

Model	J_a (meV)	J_b (meV)	J_{cS} (meV)	J_{cL} (meV)	D_b (meV)	χ_r^2
Co-best-fit	-3.17(9)	-7.31(10)	-0.57(17)	-5.11(11)	-0.47(2)	2.38

excluded in regions iii to viii due to large background contributions originating from phonons in the sample and the aluminum holder. The initial fit started with $D_b = 0$ and the YBFO DFT superexchange constants and scaled all exchange terms by a single factor to minimize the residuals using a down-hill simplex algorithm. Then, those parameters were taken as initial conditions for a least-squares fit of the extrinsic parameters along with J_a , J_b , J_{cS} , J_{cL} , and D_b , to give the **CO-best-fit** model

in Table II. A comparison of model to calculation for the **CO-best-fit** model is shown in Fig. 4 (a-h). Figure 4 (a) is the region i that is sensitive to the magnetic anisotropy, D_b . From Fig. 4 (a) to (b) to (c), the data are integrated around $L = 1$ and start around $H = K = 0.5$ and increase H from left to right, similar to data shown in the map of Fig. 3 (a) and (d). Figure 4 (d) and (e) are integrated around $L = 2$ with H around 1.3 and 1.5, respectively, similar to the maps shown in Fig. 3 (b)

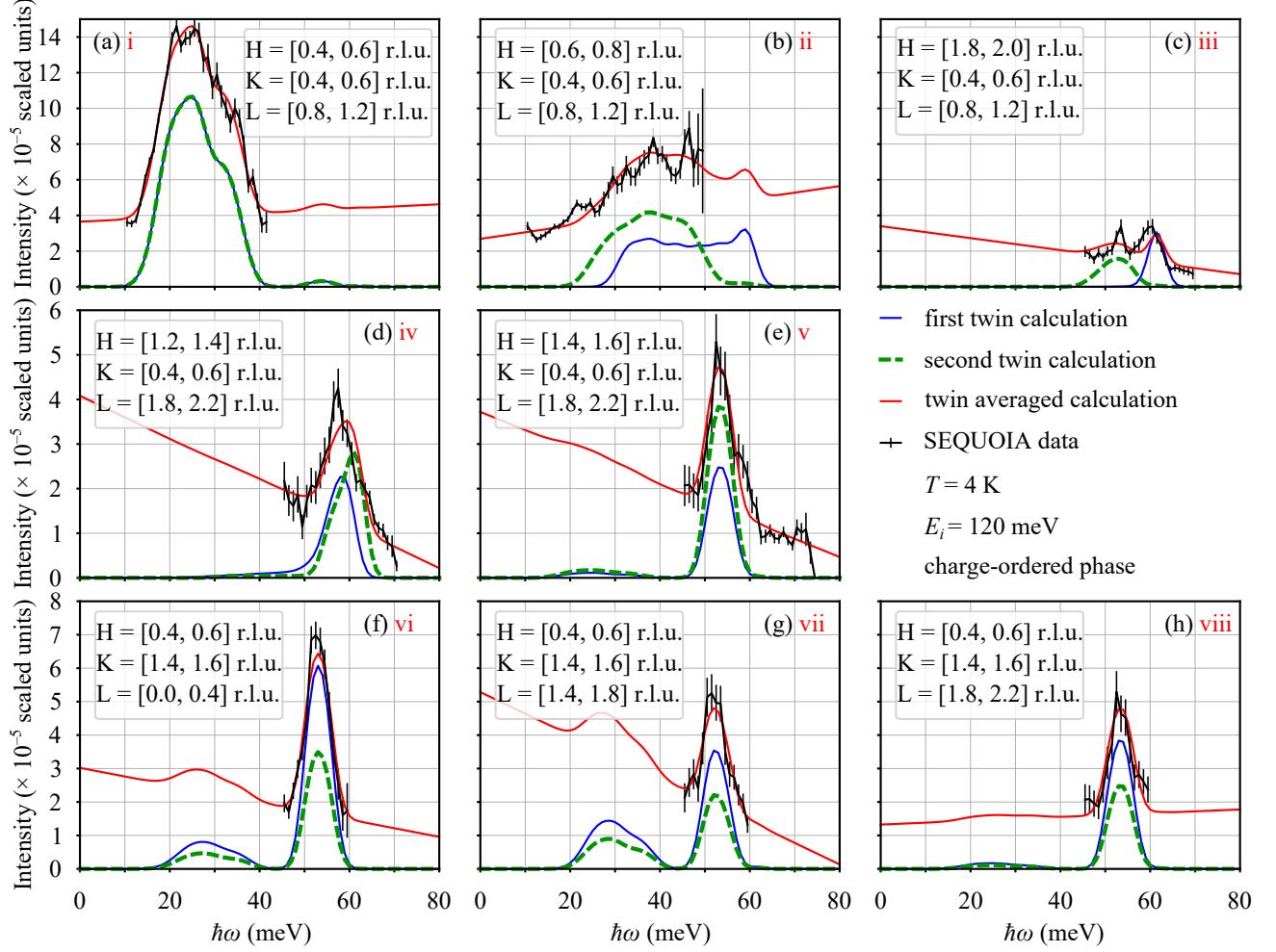


FIG. 4. Neutron scattering function intensity versus energy transfer at $T = 4$ K for TBFO in the CO phase for different \mathbf{Q} -integrations. These data were used for modeling and the **CO-best-fit** model is shown. Experimental data collected on the SEQUOIA with $E_i = 120$ meV are shown along with the calculated twin contributions and the domain averaged plus background fit. The insets of each panel show the binning range over \mathbf{Q} , which reduces the four-dimensional $S(\mathbf{Q}, \hbar\omega)$ to the one-dimensional $I(\hbar\omega)$ shown here. The red Roman numerals delineate the regions used for model optimization also shown in Fig. 3.

and (e). Fig. 4 (f) to (g) to (h) are integrated around $H = 0.5$, $K = 1.5$, with L increasing left to right, similar to the maps in Fig. 3 (c) and (f). This **CO-best-fit** model shows an easy-axis anisotropy, and all antiferromagnetic interactions. Interchanging J_{cS} and J_{cL} does not change the calculated spectrum, so the larger J_{cL} value in this model is representative of the initial conditions where the YBFO longer c-axis bond has a large superexchange energy due to bridging oxygen. However, the model is sensitive to J_{cS} and J_{cL} having these disparate values which results in intensity gaps at around 40 to 50 meV, as shown in Fig. 3 (c) and Fig. 3 (f). Alternative, less-optimal but edifying CO LSWT models for TBFO are in Appendix B. The covariance matrix of the **CO-best-fit** model is illustrated in Appendix C.

This **CO-best-fit** model is similar to that reported for YBFO powder INS in the CO phase [8], with a few key differences. The YBFO powder experiment used perturbation theory to motivate setting $J_{cS} = 0$ (defined there as J_{direct}), while these TBFO single-crystal experiments find a finite J_{cS} that is qualitatively consistent with DFT calculations of that interaction for YBFO [10]. This result implies that although $J_{direct} \approx 0$ for Fe-Fe and there is no linear link of Fe-O-Fe, the bottom four oxygen ions of the pyramidal coordination sphere can still mediate superexchange through the J_{cS} pathway. Quantitative modifications are present for the other superexchange interactions, and our data are also able to extract the magnetocrystalline anisotropy energy, which could not be determined from the YBFO powder experiment.

C. Spin waves at $T = 320$ K, above the Verwey transition

During the same experiment with the same alignment of the sample, INS was performed at $T = 320$ K, above the Verwey transition in the FV phase. Initial investigatory scans were performed with an $E_i = 240$ meV in order to ascertain the energy range of the spin waves. Subsequently, a series of single-crystal rotations with $E_i = 120$ meV were performed to extract intensities proportional to the scattering function $S(\mathbf{Q}, \hbar\omega)$. The phonon background of the sample and holder are both greatly increased at this temperature compared to the $T = 4$ K data, so the data were not folded, and analysis was focused on regions of low-momentum transfer where phonon background is minimized. Dispersive excitations were observed to originate above the FV antiferromagnetic ordering wave-vector, Fig. 5 (a-b). These data compare well to a LSWT model that is plotted for a visual comparison without any instrumental momentum resolution applied, Fig. 5 (c-d).

Aside from the change in the magnetic structure and associated LSWT parameters, an overall broadening of the spin waves is observed for TBFO in the FV phase at $T = 320$ K. This broadening requires an additional damping parameter to be included in the fitting, which is included as a gaussian broadening that is linear in energy and parameterized by Σ_{damp} . For example, if $\Sigma_{damp} = 1$ then an excitation at 20 meV has a full-width-half-max of 20 meV. Historically, phenomenological models introduce a $|\mathbf{Q}|$ -dependent damping, but recently a report on LCMO showed a deviation from that simple behavior and invoked a cut-off energy for damping [11]. Here for TBFO, a constant damping term did not reproduce the data, the addition of a quadratic damping term in energy was found to be numerically unstable, as was an energy cut-off for damping. This energy dependent damping was invoked to account for processes that cause zone-boundary spin waves to decay from magnon-magnon interactions and/or into electron conductivity channels. As the same iron 3d-electrons in the conduction band are also responsible for the magnetism, there will be some governing Hamiltonian similar to the Kondo lattice model [12].

Fitting the FV state was done by integrating over five momentum regions (i to v) and comparing to LSWT models. Operationally, the large broadening of spin waves combined with the crystallographic twinning makes separate determination of J_a and J_b unfeasible, so only the effective parameter $J_{ab} = J_a = J_b$ was used. The magnetic structure of alternately ferromagnetically coupled and antiferromagnetically coupled layers requires the constraint that $J_{cS} > 0$ and $J_{cL} < 0$, making these parameters uniquely determined in the FV phase. The overall scale-factor is taken from the $T = 4$ K model and one shared constant background term was used in the models in order to decrease the number of fitting parameters. Initial conditions were taken from the **CO-**

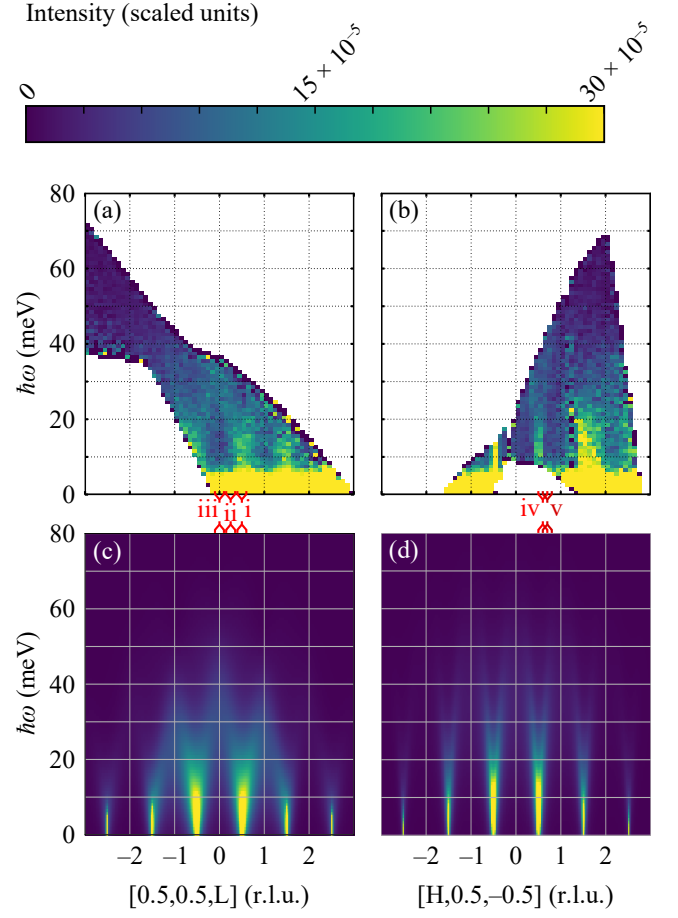


FIG. 5. Neutron scattering function intensity maps of momentum in reciprocal lattice units versus energy transfer at $T = 320$ K for TBFO in the FV phase. Experimental data collected on the SEQUOIA with $E_i = 120$ meV are shown for (a) along L such that the interval ranges are $H = [0.4, 0.6]$ r.l.u. and $K = [0.4, 0.6]$ r.l.u. and (b) along H such that $K = [0.4, 0.6]$ r.l.u. and $L = [-0.6, -0.4]$ r.l.u.. The momenta in the horizontal axis titles are the bin centers for the not-shown directions that reduce the four-dimensional $S(\mathbf{Q}, \hbar\omega)$ to the two-dimensional $S(\mathbf{Q}, \hbar\omega)$ shown here. The same regions are shown in panels (c-d) for calculations using the **FV-best-fit** parameters. The sample is twinned in the a-b plane and this twinning is included in the calculated data. These calculations use $D_b = -0.001$ meV, which accounts for the large intensity at low energies that the experimental data are not sensitive to due to the experimental energy resolution. The red Roman numerals delineate the regions used for model optimization also shown in Fig. 6.

best-fit model, except J_{cS} for which the absolute value was used. Figure 6 (a) to (b) to (c) starts at $H = K = |L| = 0.5$, and decreases $|L|$ from left to right, similar to the maps shown in Fig. 5 (a) and (c). Fig. 6 (a) to (d) to (e) starts at $H = K = 0.5$, and increases H when moving counter-clockwise, similar to the maps in Fig. 5 (b) and (d). Increasing the easy-axis D_b term (rhombic single-ion anisotropy) decreases the intensity of the low energy tail in Fig. 6 (a) and (d), which suggests $|D_b| \lesssim$

TABLE III. Linear-spin-wave-theory parameters for TBFO, $T = 320$ K data in the FV phase. The uncertainties are one standard deviation confidence intervals derived from the least-squares model. The χ_r^2 is the reduced chi squared.

Model	J_{ab} (meV)	J_{cS} (meV)	J_{cL} (meV)	D_b (meV)	D_c (meV)	Σ_{damp}	χ_r^2
FV-best-fit	-2.9(3)	1.1(7)	-2.7(3)	< -0.001 and $\gtrsim -0.1$	0.7(3)	1.0(1)	5.06

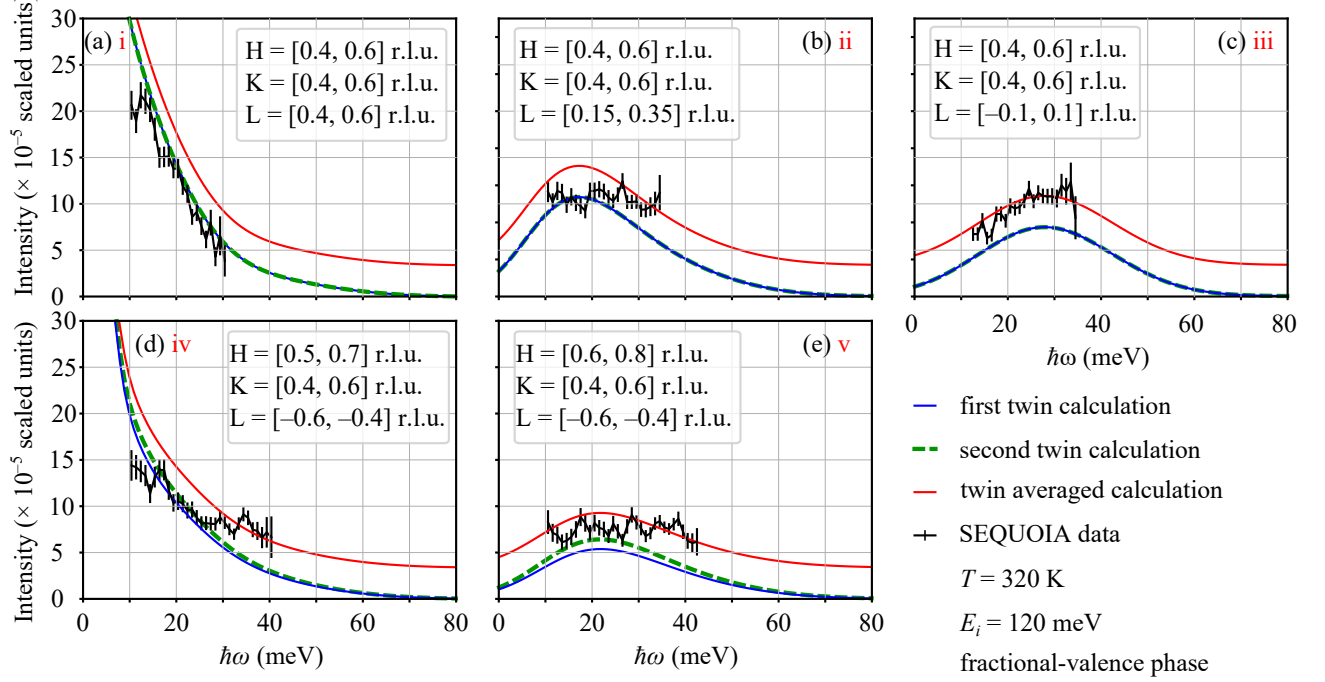


FIG. 6. Neutron scattering function intensity versus energy transfer at $T = 320$ K for TBFO in the FV phase for different \mathbf{Q} -integrations. These data were used for modeling and the **FV-best-fit** model is shown. Experimental data collected on the SEQUOIA with $E_i = 120$ meV are shown along with the calculated twin contributions and the domain averaged plus background fit. The insets of each panel show the binning range over \mathbf{Q} , which reduces the four-dimensional $S(\mathbf{Q}, \hbar\omega)$ to the one-dimensional $I(\hbar\omega)$ shown here. The red Roman numerals delineate the regions used for model optimization also shown in Fig. 5.

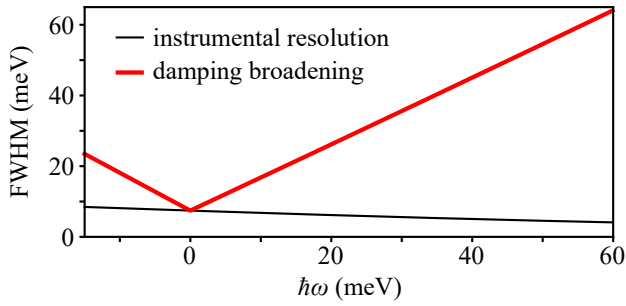


FIG. 7. Energy line-broadening from inherent instrumental effects compared to the effect of the damping in the **FV-best-fit** model.

0.1 meV [13]. The easy-plane D_c energy increases the fitness of the calculated spectra by shifting spectral weight to higher energies [13]. The broadening via Σ_{damp} required to model the data is drastically greater than the

instrumental energy resolution, Fig. 7. Alternative, less-optimal but edifying FV LSWT models for TBFO are in Appendix B. The covariance matrix of the **FV-best-fit** model is illustrated in Appendix C.

The **FV-best-fit** model allows for more quantitative fitting than was possible for the YBFO powder INS report, which was limited to extracting an overall energy scale, but also required damping to model the data [8]. Here, superexchange parameters, an easy-plane anisotropy, and a phenomenological damping parameter are determined. No calculations of the superexchange and anisotropy parameters in DCLPs in a fractional valence state are available for comparison. The damping of spin waves has been reported for a variety of systems that possess a high electrical conductivity ground-state that coexists with magnetic order, with colossal magnetoresistance manganites and metals being two important examples [14]. The ratio of the zone boundary magnon energy (E_Z) to the energy of the magnetic ordering ($k_B T_C$) has

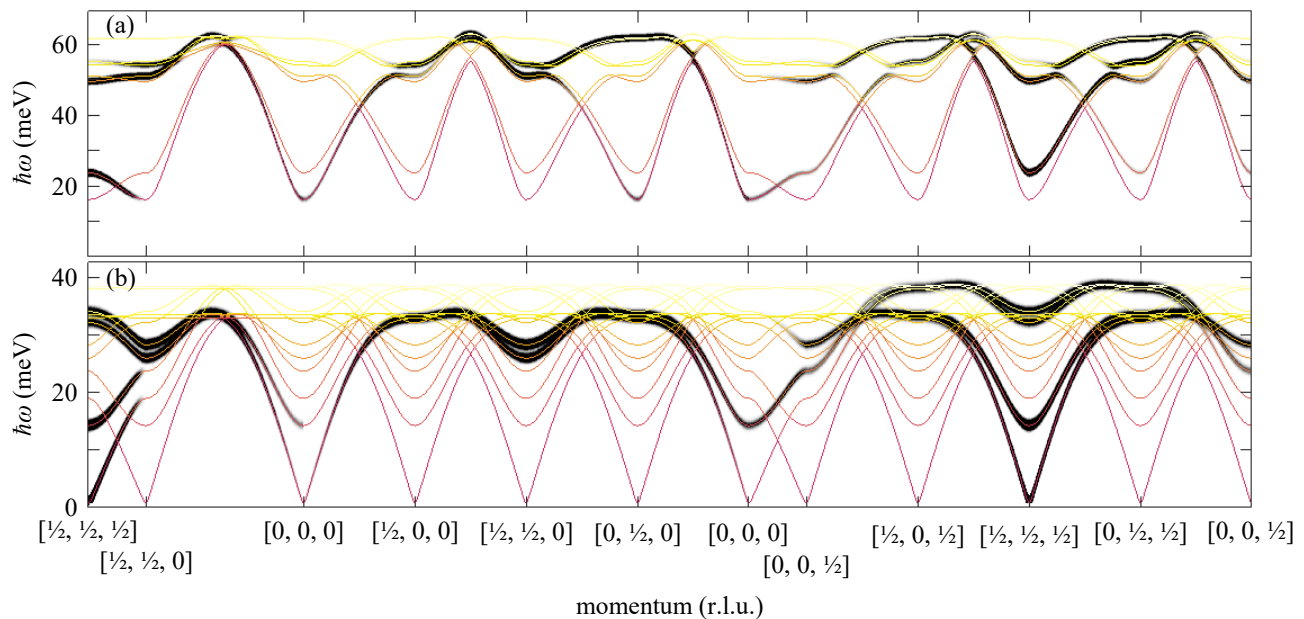


FIG. 8. Best-fit spin-wave model dispersion relationships for TBFO along high-symmetry directions in the Brillouin zone. The reciprocal lattice is pseudo-tetragonal and indexed by the INS crystallographic cell in Table I and Fig. 2 for (a) **CO-best-fit** and (b) **FV-best-fit**. The thin lines that range from red to yellow are the calculated modes and the overlaid thicker black lines show the neutron scattering intensities.

been suggested as a measure of itinerancy in the context of spin wave damping and neutron scattering. For TBFO in the FV state E_Z ranges between ≈ 25 meV and ≈ 35 meV, so dividing by $k_B T_C = 39$ meV gives a ratio of $E_Z/k_B T_C \approx 0.8$ that is smaller than the ratio for elemental Ni ($E_Z/k_B T_C = 6$) or the ratio for elemental Fe ($E_Z/k_B T_C = 9$) metals but similar to the values in optimally doped colossal-magnetoresistive (CMR) manganites ($E_Z/k_B T_C \approx 1$) [14]. The detailed physics of spin wave damping is sufficiently complex that experimental reports are limited to phenomenological fits, but these data provide a basis for more detailed theoretical treatment.

Quantitative details of the TBFO electronic structure and spin wave damping are yet to be resolved. The TBFO system is anomalous in that dominant antiferromagnetic interactions in the FV state co-exist with large damping of the excitations, as opposed to a clearly double-exchange dominated ferromagnetic system [15]. This spin wave damping in TBFO manifests itself in a similar manner for spin waves propagating in the ab-plane and along the c-axis. Comparing the **FV-best-fit** parameters to the **CO-best-fit** parameters shows a reduction in all antiferromagnetic interactions in the FV state as may be due to the introduction of ferromagnetic interactions: $\Delta J_{ab} = 2.2 \pm 0.3$ meV, $\Delta J_{cS} = 1.7 \pm 0.7$ meV, and $\Delta J_{cL} = 2.4 \pm 0.3$ meV. A Mossbauer study of YBFO [16] determined from modeling orbital populations that valence mixing takes place across the bond that we label J_{cS} in Fig. 2, which is ferromagnetic from the static magnetic structure and weakly so in our

spin wave model. Indeed, the Mossbauer derived orbital populations are consistent with first principles calculations of YBFO that showed the FV state Fermi level is dominated by iron d_z^2 orbitals [17]. So, the ferromagnetism associated with valence mixing may be a double exchange process. Taking this picture further, the existence of spin wave damping in double-cell perovskites like TBFO may be due to activated electron hopping processes in the FV state interfering with spin correlations. This type of activated hopping has been observed in GdBaFe₂O₅ (GBFO), with a characteristic activation energy of 130 meV that depends on the oxygen stoichiometry [18]. The GBFO conductivity data were analyzed to have hole-dominated conduction, which is itself puzzling in the context of the Verwey picture of charge-ordering.

Another feature of these data is the modification of magnetic anisotropy from easy-axis in CO state to easy-plane in the FV state, which is reminiscent of the modification of magnetocrystalline anisotropy in the prototypical Verwey system magnetite that goes through an isotropic point [19–21]. It may also be that the easy-plane anisotropy in the FV state is related to the similar residuals of a-axis oriented and b-axis oriented spins in the diffraction study of TBFO [6].

D. Model spin waves through the Brillouin zone

While the model optimization regions in Section II B and II C were chosen to maximize signal and avoid background, it is edifying to visualize the spin waves of **CO-**

best-fit and **FV-best-fit** along various high-symmetry directions in reciprocal space. For neutron spectroscopy of magnetic excitations, the so-called magnetic interaction vector ($\mathbf{Q} \times \mathbf{S} \times \mathbf{Q}$) scales the detected intensity by the component of the magnetic moment that is perpendicular to the scattered momentum. These model modes and INS intensities are shown in Fig. 8. For this plot, the **CO-best-fit** calculations are not twinned so that the a- and b-directions are unique. Unlike experimental data, for which energy and momentum are always binned over finite intervals, purely theoretical calculations have no such restriction and Fig. 8 displays infinitely thin slices.

III. CONCLUSIONS AND OPEN QUESTIONS

We have measured and modeled the spin wave excitations in TbBaFe₂O₅ (TBFO) in the charge ordered (CO) state at $T = 4$ K and in the fractional valence (FV) state at $T = 320$ K using single crystal inelastic neutron scattering. While the Verwey transition was observed a century ago, the detailed concepts remain contentious. So, the parameters we extracted may be used to compare with electronic structure calculations to improve understanding of FV to CO transitions in transition metal oxides. The magnetic anisotropy is easy-axis in the CO state and changes to easy-plane in the FV state. The FV state shows strong spin wave damping that is associated with the large electronic conductivity in that phase, but detailed microscopic models are lacking for the specific class of double layered perovskites. It will also be interesting to see how magnetic Monte Carlo simulations of bulk properties informed by the model parameters reported herein may reproduce reported measurements.

ACKNOWLEDGMENTS

D. M. Pajerowski, S. E. Hahn, W. Tian, G. E. Granroth, and A. I. Kolesnikov are supported through the Scientific User Facilities Division of the Department of Energy (DOE) Office of Science, sponsored by the Basic Energy Science (BES) Program, DOE Office of Science. Work at the Ames Laboratory was supported by the U.S. Department of Energy (USDOE), Office of Basic Energy Sciences, Division of Materials Sciences and Engineering. Ames Laboratory is operated for the USDOE by Iowa State University under Contract No. DE-AC02-07CH11358. This research used resources at the Spallation Neutron Source, a DOE Office of Science User Facility operated by the Oak Ridge National Laboratory. We acknowledge Lisa DeBeer-Schmitt for help setting up the experiment, and Matthieu Doucet for conversations about model fitness. This manuscript has been authored by UT-Battelle, LLC under Contract No. DE-AC05-00OR22725 with the U.S. Department of Energy. The United States Government retains and the publisher, by accepting the article for publication,

acknowledges that the United States Government retains a non-exclusive, paid-up, irrevocable, world-wide license to publish or reproduce the published form of this manuscript, or allow others to do so, for United States Government purposes. The Department of Energy will provide public access to these results of federally sponsored research in accordance with the DOE Public Access Plan (<http://energy.gov/downloads/doe-public-access-plan>).

Appendix A: Technical details

The TBFO sample was grown using the floating-zone technique using an infrared image furnace with details as in reference [7]. For the neutron experiments, ≈ 0.3 grams crystals were co-aligned on aluminum mounts. Cryogenic temperatures were achieved with a wet ⁴He cryostat. The time-of-flight spectrometer at the SNS BL-17 (SEQUOIA) [22, 23] was used with $E_i=120$ meV, Fermi 1=300 Hz, and T0=90 Hz, and with $E_i=240$ meV, Fermi 1=360 Hz, and T0=120 Hz. E_i is the incident energy of the neutron radiation. Energy transfer from the neutron to the sample is denoted as $\hbar\omega$ and momentum transfer from the neutron to the sample is reported in reciprocal lattice units (r.l.u.). Experimental energy resolutions are from MANTID [24], such that for the $E_i=120$ meV data the energy resolution is well modeled by the polynomial expansion in energy transfer: $\text{FWHM (meV)} = (3.115 \times 10^{-7} \text{ meV}^{-2})(\hbar\omega)^3 + (1.6792 \times 10^{-4} \text{ meV}^{-1})(\hbar\omega)^2 - (6.6751 \times 10^{-2})(\hbar\omega) + 7.4289 \text{ meV}$. The data were normalized to the proton current on target during collection. Data were collected at SNS power of ≈ 700 kW for ≈ 30 minutes/angle (1.0 Coulombs of proton charge per angle) and ≈ 45 minutes/angle (1.5 Coulombs of proton charge per angle) for the $T = 4$ K and $T = 320$ K data, respectively. The detectors were normalized using a vanadium standard measurement that is defined to have an average intensity per pixel of 1 scaled unit. The single-crystal was rotated in the HHL plane in increments of 2 degrees about the vertical axis, with the resulting intensity scaled by incident momentum divided by final momentum in order to generate the four-dimensional $S(H, K, L, \hbar\omega)$ scattering function. Linear-spin-wave-theory calculations [25] were performed using SpinWaveGenie, [26] and a Bose factor correction is applied to the spin wave intensities to account for temperature changes in single-magnon states. Subsequent to parameter optimization, Fig. 8 was generated with SpinW [27]. All numerical optimizations used the libraries of SciPy. [28]

Appendix B: Relevant, less-optimal models

In Section II the optimal models for the CO and FV phases were presented as **CO-best-fit** and **FV-best-fit**, respectively. However, other models were tried that both

TABLE IV. Linear-spin-wave-theory parameters for TBFO, $T = 4$ K data in the CO phase. The uncertainties are one standard deviation confidence intervals derived from the least-squares model. The χ_r^2 is the reduced chi squared.

Model	J_a (meV)	J_b (meV)	J_{cS} (meV)	J_{cL} (meV)	D_b (meV)	χ_r^2
CO-2	-3.25(3)	-7.27(10)	-3.06(5)	-3.06(5)	-0.30(2)	3.53
CO-3	-5.13(5)	-5.13(5)	-0.58(21)	-5.39(13)	-0.43(3)	2.73

TABLE V. Linear-spin-wave-theory parameters for TBFO, $T = 320$ K data in the FV phase. The uncertainties are one standard deviation confidence intervals derived from the least-squares model. The χ_r^2 is the reduced chi squared, and χ_r^{*2} has the energy range of optimization for Fig. 6 (c-d) limited to greater than 20 meV. The rows that are offset below the **FV-2** and **FV-3** models correspond to evaluation in the modified energy range as for the χ_r^{*2} definition.

Model	J_{ab} (meV)	J_{cS} (meV)	J_{cL} (meV)	D_b (meV)	D_c (meV)	Σ_{damp}	χ_r^2	χ_r^{*2}
FV-1	-2.9(3)	1(3)	-2.7(5)	0(6)	1(2)	1.0(1)	5.10	
FV-2 (FV-best-fit)	-2.9(3)	1.1(7)	-2.7(3)	-0.1	0.7(3)	1.0(1)	5.06	
	-2.9(2)	1(1)	-2.7(3)	-0.1	0.7(5)	1.0(1)		3.86
FV-3	-2.7(4)	0.1(1)	-2.4(4)	-0.1	0.027(3)	2.2(6)	2.80	
	-2.7(4)	0.1(2)	-2.4(5)	-0.1	0.0(2)	2.2(7)		2.91
FV-3*	-2.2(2)	0.00(1)	-2.5(3)	-0.1	1.4(6)	1.1(1)		2.31

support the chosen parameter sets and illustrate potential ambiguities.

Consider first the $T = 4$ K CO data. For a **CO-2** model that forces $J_{cS} = J_{cL}$, the result is essentially an average of the individually varied parameters, the intensity gaps along the L direction are not reproduced, and the goodness of fit decreases, Table IV, although the other parameters are only marginally affected. For a **CO-3** model that forces $J_a = J_b$, the qualitative features of the experimental data are still reproduced by the model, but there is still a slightly decreased fit quality, able IV. For **CO-3**, there is only one mode in the analogous scan to Fig. 3 (d). Indeed, to more clearly extricate the J_a and J_b parameters, an un-twinned sample would have to be measured. Of the models considered, the **CO-best-fit** has the smallest χ_r^2 .

The FV data at $T = 320$ K were numerically trickier due to the small excitation gap along with the fact that the intensity of classical antiferromagnetic spin waves varies $\sim \frac{1}{\hbar\omega}$. First, the model **FV-1** included J_{ab} , J_{cS} , J_{cL} , D_b , D_c , and Σ_{damp} was optimized and large parameter (co)variance developed for J_{cS} , D_b , and D_c . The b-axis anisotropy D_b trending to zero is consistent with the observation of no excitation gap within experimental energy resolution. In addition, there is an additional complication that the ground-state magnetic structure of Fig. 2 (b) is not well-defined when $|D_b| < 0.001$ meV, causing the LSWT intensities to diverge at low energies due zero energy spin rotations in the ab-plane. So, the model **FV-2 (FV-best-fit)** uses the parameters from **FV-1** and does not vary D_b , which removes the large (co)variances in the solution. Lastly, the model **FV-3** takes the **FV-2 (FV-best-fit)** model and then allows D_c to also vary. While the **FV-3** model has the best fit according to the χ_r^2 in Table V, this apparent improved fitness is due to a better fit in the poorly determined low energy region near the magnetic Bragg peak that

dominates the residuals due to the large intensity contribution. Conversely, the minimization of **FV-1** partially avoids this region near the magnetic ordering wave-vector in the fitting as the numerics of the LSWT for this model has divergences for energy transfers less than 17 meV and the minimizer becomes insensitive to those specific data.

There is a degree of arbitrariness in selecting the momentum binning and energy ranges to use in these fits that is based upon a by-eye determination of magnetic intensity, so we leave the binning ranges as determined and then the **FV-best-fit** parameter set does not have the lowest χ_r^2 as defined by those more-model-agnostically chosen ranges. Indeed, manually reducing the energy range to < 20 meV for the optimization for the **FV-3*** model shows how the D_c anisotropy parameter recovers under such conditions. For this decreased energy range, the goodness-of-fit parameter χ_r^{*2} is introduced. It is interesting that this manual intervention does not capture the data as well as the **FV-1** model, as the **FV-3** and **FV-3*** models have decreased χ_r^{*2} but in fact have qualitative disagreements with the experimental data (again due to low $\hbar\omega$ dominating the residuals),[13] so the minimization algorithm is apparently robust in this case even when the intensities have divergences.

Appendix C: best-fit model parameter covariance

In the main text, parameter likelihoods are captured by reporting the standard deviation of the least-squares fitting results. Additional information regarding the model behavior is captured in the covariance matrix, from which the reported uncertainties in Tables II and III are derived via the square root of the diagonal elements. The covariance is a measure of the mutual variability of two parameters within a given model to achieve a likely solution. A positive covariance in this context means two parameters

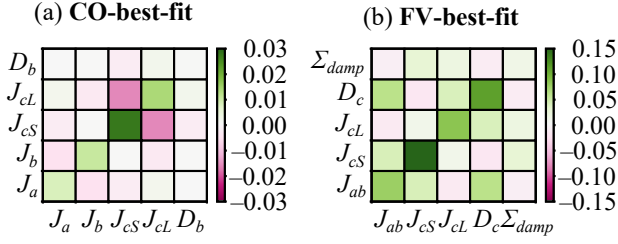


FIG. 9. Intensity maps of the covariance matrices for the best-fit spin wave models. Units are as reported in the text. The $[J_{cS}, J_{cS}]$ value for **FV-best-fit** is off-scale at nearly 0.5 meV^2 .

both increasing can give an equally likely solution, while a negative covariance means if one parameter increases and the other decreases then an equally likely solution may be achieved. This concept is related to the ellipticity of the χ^2_r surface in parameter space. For an ideally well-behaved model, the diagonal elements of the covariance matrix will be significantly larger than the off-diagonal elements. These covariance matrices have been normalized, and therefore the elements directly correspond to

the bilinear parameter correlation coefficients.

Illustrations of the covariance matrices by gridded heatmaps for the intrinsic parameters of the **CO-best-fit** and **FV-best-fit** models are shown in Fig. 9. For the **CO-best-fit** model, the largest off-diagonal elements as compared to the magnitude of the diagonal elements for a given parameter are for $[J_a, J_b]$ and $[J_{cS}, J_{cL}]$, and both are negative. Explicitly stated for $[J_a, J_b]$, this value means that there are models where J_a increases with J_b decreasing that have similar likelihoods to the optimal model. Conversely, for the **FV-best-fit** model $[J_{cS}, J_{cL}]$ is much smaller than either $[J_{cS}, J_{cS}]$ or $[J_{cL}, J_{cL}]$ and so those parameters are more uniquely determined in the context of standard deviations from the best-fit mean. In **FV-best-fit**, $[J_{ab}, D_c]$ shows a relatively large positive covariance as both parameters can shift intensities at the zone boundary to higher energies. Also, the Σ_{damp} parameter has a relatively significant covariance with all other model parameters compared to the diagonal element, which itself is only 10% of the mean. Generally speaking, these models are well behaved as the off-diagonal elements are comparatively small, even in the cases highlighted as potentially ambiguous for these models.

-
- [1] D. I. Khomskii and G. A. Sawatzky, Interplay between spin, charge and orbital degrees of freedom in magnetic oxides, *Solid State Communications* **102**, 87 (1997).
 - [2] F. Walz, The Verwey transition - A topical review, *Journal of Physics Condensed Matter* **14** (2002).
 - [3] J. García and G. Subías, The Verwey transition - A new perspective, *Journal of Physics Condensed Matter* **16** (2004).
 - [4] D. O. Smith, Magnetization of a magnetite single crystal near the curie point, *Phys. Rev.* **102**, 959 (1956).
 - [5] P. Karen and P. M. Woodward, Synthesis and structural investigations of the double perovskites $REBaFe_2O_{(5+w)}$ ($RE=Nd, Sm$), *Journal of Materials Chemistry* **9**, 789 (1999).
 - [6] P. Karen, P. M. Woodward, J. Lindén, T. Vogt, A. Studer, and P. Fischer, Verwey transition in mixed-valence $TbBaFe_2O_5$: Two attempts to order charges, *Phys. Rev. B* **64**, 214405 (2001).
 - [7] D. K. Pratt, S. Chang, W. Tian, A. A. Taskin, Y. Ando, J. L. Zarestky, A. Kreyssig, A. I. Goldman, and R. J. McQueeney, Checkerboard to stripe charge ordering transition in $TbBaFe_2O_5$, *Phys. Rev. B* **87**, 045127 (2013).
 - [8] S. Chang, P. Karen, M. P. Hehlen, F. R. Trouw, and R. J. McQueeney, Damping of antiferromagnetic spin waves by valence fluctuations in the double layer perovskite $YBaFe_2O_5$, *Phys. Rev. Lett.* **99**, 037202 (2007).
 - [9] K. Momma and F. Izumi, VESTA 3 for three-dimensional visualization of crystal, volumetric and morphology data, *Journal of Applied Crystallography* **44**, 1272 (2011).
 - [10] Y. Zhang and M. H. Whangbo, Density functional analysis of the spin exchange interactions and charge order patterns in the layered magnetic oxides $YBaM_2O_5$ ($M = Mn, Fe, Co$), *Inorganic Chemistry* **50**, 10643 (2011).
 - [11] J. S. Helton, S. K. Jones, D. Parshall, M. B. Stone, D. A. Shulyatev, and J. W. Lynn, Spin wave damping arising from phase coexistence below T_c in colossal magnetoresistive $La_{0.7}Ca_{0.3}MnO_3$, *Phys. Rev. B* **96**, 104417 (2017).
 - [12] C. Zener, Interaction between the d-shells in the transition metals. II. Ferromagnetic compounds of manganese with Perovskite structure, *Phys. Rev.* **82**, 403 (1951).
 - [13] See Supplemental Material at [URL will be inserted by publisher] for some additional details of the fractional valence (FV) spin wave model.
 - [14] T. Chatterji, *Neutron scattering from magnetic materials*, 1st ed. (Elsevier, Boston, 2006).
 - [15] D. I. Golosov, Spin wave theory of double exchange ferromagnets, *Phys. Rev. Lett.* **84**, 3974 (2000).
 - [16] J. Lindén, F. Lindroos, and P. Karen, Orbital occupancy evolution across spin- and charge-ordering transitions in $YBaFe_2O_5$, *Journal of Solid State Chemistry* **252**, 119 (2017).
 - [17] C. Spiel, P. Blaha, and K. Schwarz, Density functional calculations on the charge-ordered and valence-mixed modification of $YBaFe_2O_5$, *Phys. Rev. B* **79**, 115123 (2009).
 - [18] J. Lindén, P. Karen, J. Nakamura, M. Karppinen, and H. Yamauchi, Transport and magnetotransport properties across the two-step Verwey transition in $BaGdFe_2O_{5+w}$, *Phys. Rev. B* **73**, 064415 (2006).
 - [19] L. R. Bickford, J. M. Brownlow, and R. F. Penoyer, Magnetocrystalline anisotropy in cobalt-substituted magnetite single crystals, *Proceedings of the IEE - Part B: Radio and Electronic Engineering* **104**, 238 (1956).
 - [20] M. Yama-ai, M. Ozima, and T. Nagata, Self-reversal of Remanent Magnetization of Magnetite at Low Temperatures, *Nature* **198**, 1188 (1963).

- [21] M. Blackman, G. Haigh, and N. D. Lisgarten, On the Magnetic Transformation and the Domain Structure of Magnetite, [Proc. Phys. Soc. Lond. **81**, 244 \(1963\)](#).
- [22] G. E. Granroth, D. H. Vandergriff, and S. E. Nagler, SEQUOIA: A fine resolution chopper spectrometer at the SNS, [Physica B: Condensed Matter **385-386**, 1104 \(2006\)](#).
- [23] G. E. Granroth, A. I. Kolesnikov, T. E. Sherline, J. P. Clancy, K. A. Ross, J. P. Ruff, B. D. Gaulin, and S. E. Nagler, SEQUOIA: A newly operating chopper spectrometer at the SNS, [Journal of Physics: Conference Series **251** \(2010\)](#).
- [24] O. Arnold, J. C. Bilheux, J. M. Borreguero, A. Buts, S. I. Campbell, L. Chapon, M. Doucet, N. Draper, R. F. Leal, M. A. Gigg, V. E. Lynch, A. Markvardsen, D. J. Mikkelsen, R. L. Mikkelsen, R. Miller, K. Palmen, P. Parker, G. Passos, T. G. Perring, P. F. Peterson, S. Ren, M. A. Reuter, A. T. Savici, J. W. Taylor, R. J. Taylor, R. Tolchenov, W. Zhou, and J. Zikovsky, Nuclear Instruments and Methods in Physics Research A Mantid Data analysis and visualization package for neutron scattering and μ SR experiments, [Nuclear Inst. and Methods in Physics Research, A **764**, 156 \(2014\)](#).
- [25] J. T. Haraldsen and R. S. Fishman, Spin rotation technique for non-collinear magnetic systems: Application to the generalized Villain model, [Journal of Physics Condensed Matter **21** \(2009\)](#).
- [26] S. E. Hahn, R. S. Fishman, and G. Ehlers, [SpinWaveGenie](#) (2019).
- [27] S. Toth and B. Lake, Linear spin wave theory for single-Q incommensurate magnetic structures, [Journal of Physics Condensed Matter **27** \(2015\)](#).
- [28] E. Jones, T. Oliphant, and P. Peterson, [SciPy: Open source scientific tools for Python](#) (2001).